



Cite this: *React. Chem. Eng.*, 2021, 6, 1928

## Enhanced methane conversion using Ni-doped calcium ferrite oxygen carriers in chemical looping partial oxidation systems with CO<sub>2</sub> utilization

Vedant Shah,<sup>†</sup> Zhuo Cheng, <sup>†</sup> Pinak Mohapatra and Liang-Shih Fan <sup>\*</sup>

Chemical looping partial oxidation (CLPO) is a novel technology for converting methane into high quality syngas that can be further converted into liquid fuels. In the present work, Ni-doped Ca<sub>2</sub>Fe<sub>2</sub>O<sub>5</sub> oxygen carriers are employed as looping media wherein the Ni-doping concentration is varied from 0 to 10%. Thermogravimetric performance tests are carried out where the doped/undoped carriers are subjected to methane reduction in the first half cycle and subsequently the reduced carriers are regenerated using CO<sub>2</sub> or air in the second half. The cyclic redox performance of Ni doping on the characteristics and the stabilities of these oxygen carriers are also investigated by means of X-ray diffraction and scanning electron microscopy. Based on the oxygen carrier characterization, an unwanted phase, NiFe<sub>2</sub>O<sub>4</sub>, is formed beyond 5% dopant concentration which exhibited weak methane interaction and inhibited CO<sub>2</sub> regeneration thermodynamically. Moreover, doping Ni at 0–5% exhibited increased reactivity across the temperature range of 750–1000 °C as compared to the undoped sample, with the 5% Ni doped sample showing a substantial improvement of 1149% over the undoped sample at 750 °C. This explains its potential in an adiabatic process where a temperature gradient is generally observed across the syngas generation reactor. Density functional theory (DFT) calculations further reveal the role of the Ni doping effect on methane partial oxidation and CO<sub>2</sub> conversion, wherein adding the Ni dopant lowers the oxygen vacancy formation energy and increases the CO<sub>2</sub> adsorption energy which is favorable for CO<sub>2</sub> activation and splitting. The findings of this study provide a fundamental insight into the reactivity enhancement of calcium ferrite-based oxygen carriers and open new avenues for designing a novel chemical looping system for simultaneous syngas generation and CO<sub>2</sub> utilization.

Received 16th April 2021,  
Accepted 30th June 2021

DOI: 10.1039/d1re00150g

rsc.li/reaction-engineering

### 1. Introduction

Abundance of shale reserves in the U.S. has propelled the extraction of natural gas at unprecedented rates. Coupled with the lowering of prices and an increase in the energy demand, natural gas utilization is at an all-time high.<sup>1</sup> Natural gas has already surpassed coal as the fuel utilized in thermal power stations for producing electricity.<sup>2</sup> Methane, which constitutes the majority of the natural gas by volume, is an extremely versatile compound, serving as the building block of petrochemical industry. Apart from its use as a fuel in the conventional sense, it is also used for producing value-added products of commercial importance. An example of such a process is the oxidative coupling of methane (OCM)

where methane is converted into higher hydrocarbons in a single step.<sup>3</sup> However, this type of methane utilization has numerous practical challenges such as deactivation of catalysts due to coking, low per pass fuel conversion and low-to-moderate product yields. Moreover, separation of CO/CO<sub>2</sub> gases from the product hydrocarbon feed is energy intensive. Consequently, a more common route for converting natural gas/shale gas/methane into syngas is adopted in the industry, wherein the syngas produced is further processed to generate desirable products.

Syngas production has been conventionally carried out using processes such as steam methane reforming (SMR) or autothermal reforming (ATR) wherein the natural gas is co-fed into a reformer with steam and/or molecular oxygen for partial oxidation.<sup>4</sup> Moreover, processes such as dry methane reforming (DMR) and catalytic partial oxidation of methane (CPOX) are being actively investigated for their commercial deployment. Methane is reformed using CO<sub>2</sub> and molecular O<sub>2</sub> in the presence of a catalyst in the DRM and CPOX

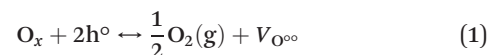
William G. Lowrie Department of Chemical and Biomolecular Engineering, The Ohio State University, 151 West Woodruff Avenue, Columbus, OH 43210, USA.  
E-mail: fan.1@osu.edu; Tel: +614 688 3262

<sup>†</sup> These authors contributed equally to this work.

processes, respectively.<sup>5</sup> However, all the above mentioned processes collectively suffer from limitations such as high endothermic heat requirement, catalyst deactivation due to coking, and added CO<sub>2</sub> capture cost that arises from burning tail gases and additional fuel for providing heat to the reformer.<sup>6,7</sup> Additionally, most of the total parasitic energy required to operate these processes is consumed by the cryogenic air separation unit (ASU), which increases the operating cost requirement.<sup>8</sup> As CO<sub>2</sub> generation along with its capture remains a major concern in the industry, several techniques including amine-based removal, membrane-based separation, or sorbent-based capture are employed to achieve the goal of carbon capture, utilization and storage (CCUS). However, the primary concern with these processes is their high energy and cost demand, thus making it imperative to develop technologies that can achieve this goal in a more economic and sustainable manner.

Chemical looping partial oxidation (CLPO) is an advanced technology that offers the advantage of converting methane into syngas in an efficient and clean manner while mitigating the drawbacks associated with conventional syngas production technologies. In chemical looping, metal oxides and their derivatives serve as oxygen sources where the lattice oxygen present within these oxides is responsible for selectively oxidizing methane to produce syngas.<sup>9,10</sup> The reduced metal oxides are then regenerated using air in a separate reactor, thus eliminating the need for an ASU as no molecular oxygen is required. The fundamental scheme of a CLPO process is depicted in Fig. 1, wherein a two-reactor system is employed for syngas production. The movement of oxygen ions present in the oxygen carrier lattice takes place due to the interaction between gaseous oxygen and the oxygen vacancies as shown in reaction (1), where  $V_{O^{\bullet\bullet}}$  is the

oxygen vacancy,  $O_x$  is the location of the oxygen ion in the lattice and  $h$  is the electron hole.



Apart from the role of oxygen carriers in selectively oxidizing natural gas to produce syngas instead of full combustion products (CO<sub>2</sub>/H<sub>2</sub>O), the mode of gas–solid contact in the reducer remains critical. The syngas produced using a fluidized bed reducer has a lower purity as the solid conversion (extent of lattice oxygen lost to methane) is not uniform across all the particles, and as a result syngas can be overoxidized to produce a higher concentration of CO<sub>2</sub>/H<sub>2</sub>O.<sup>5</sup> A high-purity syngas stream can be produced by using a co-current moving bed reducer configuration wherein both CH<sub>4</sub> and the oxygen carrier particles move downwards along the length of the reducer and the syngas produced through gas–solid equilibrium exits the reducer from the bottom as depicted in Fig. 1.<sup>11</sup> This type of reactor configuration ensures all the particles undergo a similar extent of reduction, thus preventing overoxidation of syngas.

Oxygen carriers are the most critical component of the CLPO process as their performance dictates the process economics. They must be developed such that their activity is retained across an extended number of redox cycles and at the same time show a higher tolerance towards attrition.<sup>12</sup> Although the oxides of several transition elements show multiple oxidation states (and thus redox capable), both supported and unsupported Fe-based oxides remain the preferred choice due to their good reaction kinetics, high mechanical strength, and low procurement cost.<sup>13,14</sup> However, pure Fe-based metal oxides do not show very high activity towards methane to produce syngas. As a result, Fe<sub>2</sub>O<sub>3</sub> is typically combined with either support(s), dopant(s), or a combination of both for reactivity enhancement. Addition of dopants such as Cu and Co to Fe<sub>2</sub>O<sub>3</sub> has shown considerable improvement in reactivity towards CH<sub>4</sub>, especially at low temperatures.<sup>15,16</sup> More recently, the use of Fe<sub>2</sub>O<sub>3</sub>-based nanosized oxygen carriers developed by Liu *et al.* showed near 100% selectivity towards CO formation along with a substantial improvement in the reactivity as compared to the unsupported, microsized Fe<sub>2</sub>O<sub>3</sub>.<sup>17</sup> The use of Fe-based perovskites for carrying out partial oxidation of methane to generate syngas has also been reported in the literature, wherein the perovskites offer inherent advantages of high oxygen mobility and better control over the product selectivity by doping either A or B sites of the crystal. For instance, Zhang *et al.* have reported that partially substituting La with Ce in LaFeO<sub>3</sub> promotes methane conversion while also boosting the performance of water splitting during the regeneration of the reduced carrier.<sup>18</sup> The authors have also reported an increase in the syngas yield and CO<sub>2</sub> conversion (during regeneration) for the La<sub>0.5</sub>Ce<sub>0.5</sub>FeO<sub>3</sub> oxygen carrier due to a higher distortion of FeO<sub>6</sub> octahedra as compared to pure LaFeO<sub>3</sub>.<sup>19</sup> Another approach for improving oxygen

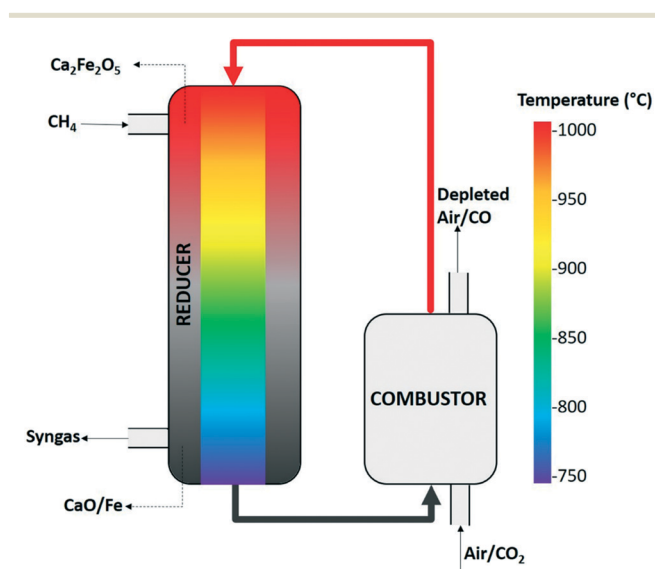


Fig. 1 A schematic of the adiabatic chemical looping partial oxidation process for syngas generation depicting a temperature gradient in the reducer.

carrier reactivity is the coupling of CaO and Fe<sub>2</sub>O<sub>3</sub> to form Ca<sub>2</sub>Fe<sub>2</sub>O<sub>5</sub>, an active metal oxide with a unique brownmillerite structure that can undergo cyclic redox reactions.<sup>20</sup> Ca<sub>2</sub>Fe<sub>2</sub>O<sub>5</sub> exhibits high reactivity due to the presence of oxygen ion vacancies in the structure, which accelerate the rates of ion dissemination through intervacancy diffusion.<sup>21</sup> Apart from better reaction kinetics, Ca<sub>2</sub>Fe<sub>2</sub>O<sub>5</sub> also exhibits a high thermodynamic selectivity towards partial oxidation as reported by Shah *et al.*, wherein the production of syngas with a purity of >98% along with almost-complete CH<sub>4</sub> conversion is reported.<sup>22,23</sup> Due to its kinetic and thermodynamic benefits, the use of Ca<sub>2</sub>Fe<sub>2</sub>O<sub>5</sub> for producing syngas and hydrogen by carrying out partial oxidation of various feedstocks such as biomass, coal, risk husk, coal tar vapor, microalgae and CH<sub>4</sub> has been reported by various research groups.<sup>24–30</sup> The effect of adding dopants and supports has been investigated. Their addition to Ca<sub>2</sub>Fe<sub>2</sub>O<sub>5</sub> has been reported to enhance the reaction rates. Liu *et al.* reported that substituting Ca atoms with Sr in the lattice enhanced the Fe<sup>3+</sup> activity in Ca<sub>2</sub>Fe<sub>2</sub>O<sub>5</sub>, whereas doping with Co led to an improvement in the hydrogen yield for biomass gasification.<sup>28,31</sup> Hosseini *et al.* investigated the role of Cu and Ni dopants and concluded that rapid formation of metallic Ni/Cu through exsolution promoted Ca<sub>2</sub>Fe<sub>2</sub>O<sub>5</sub> reducibility in CH<sub>4</sub>.<sup>32</sup> The effect of supports such as MgO, ZnO, and Al<sub>2</sub>O<sub>3</sub> on Ca<sub>2</sub>Fe<sub>2</sub>O<sub>5</sub> reactivity has been reported by Liu *et al.* who concluded that MgO was a superior support material as it increased the oxygen release capability of Ca<sub>2</sub>Fe<sub>2</sub>O<sub>5</sub> for partial oxidation of biomass to produce syngas.<sup>33</sup>

For all the studies reported in the literature, the reducer is typically operated isothermally at high temperatures and as a result, the rates of reaction remain high. However, a commercial CLPO process must be operated adiabatically to significantly reduce the cost associated with providing an external endothermic heat to the system. An adiabatic CLPO system is the one where the heat generated in the combustor during the regeneration of reduced oxygen carriers is transferred to the reducer and utilized for carrying out the endothermic partial oxidation reaction.<sup>34</sup> As the reactor operates adiabatically without any external heat to drive the reaction, a temperature gradient is established in the reducer along its length where the top is at a higher temperature whereas the bottom is at low temperature as shown in Fig. 1, and the gradient is developed as the reaction progresses in the absence of any external heating and the temperature drops from 1000 to 750 °C. CH<sub>4</sub> shows a good reactivity at high temperatures due to enhanced kinetics, but the rate of reaction slows down as the temperature drops. As a result, it is important to develop an oxygen carrier that can enhance CH<sub>4</sub> conversion even at low temperatures. Although extensive research has been conducted on modifying oxygen carriers with various dopants for their reactivity enhancement, much work remains to be done in terms of exploring the dopant effect on the structure/activity relationship. A deeper understanding of the underlying enhancement mechanism is also crucial for the design of highly active and stable oxygen

carriers. The work reported here focuses on the use of Ni-doped Ca<sub>2</sub>Fe<sub>2</sub>O<sub>5</sub> carriers for the CLPO process. The role of Ni doping in this study has been systematically examined using density functional theory (DFT)-combined experimental investigation to gain a mechanical insight into the reactivity of calcium ferrite oxygen carriers in this process. The regeneration of reduced calcium ferrite using CO<sub>2</sub> has also been investigated as the reduced Ca<sub>2</sub>Fe<sub>2</sub>O<sub>5</sub> possesses a unique ability to be fully regenerated in CO<sub>2</sub>. The regeneration involves the production of CO which is an important industrial commodity used for numerous applications like manufacturing of chemicals (acids, esters, alcohols, *etc.*) and synthesizing metal carbonyls, and in the pharmaceutical industry and electronics and semiconductors.<sup>35</sup>

## 2. Experimental and computational details

### 2.1 Sample preparation and characterization

Five polycrystalline Ca<sub>2</sub>Fe<sub>2-x</sub>Ni<sub>x</sub>O<sub>5</sub> samples with  $x = 0, 0.01, 0.02, 0.05,$  and  $0.1$  were prepared using the solid-state synthesis technique. Powders of CaO (Fischer Scientific, 99+%), Fe<sub>2</sub>O<sub>3</sub> (Noah Technologies Corporation, 99.9%), and NiO (Noah Technologies Corporation, 99.9%) were mixed in the desired proportions and subjected to dry ball milling for 8 hours to obtain a homogeneous powder mixture. The mixture was converted into a thick, viscous paste by adding DI water. This paste was dried overnight and crushed to form a powder, which was calcined at 1150 °C for 6 hours to obtain the oxygen carrier sample. Heating and cooling rates of 2 °C min<sup>-1</sup> were maintained during the calcination sequence. The as-obtained calcined sample was sieved to obtain particles in the size range of 125–250 μm, which were used for all further experiments. All the solid samples were subjected to scanning electron microscopy (SEM) and X-ray diffraction (XRD) for characterizing the sample morphology and the phases formed because of the interaction between the different metal oxide constituents. The SEM images were obtained using a Quanta 200 electron microscope under high-vacuum setting with the accelerating voltage, emission current, and working distance set to 10 kV, 100 μA, and 13 mm, respectively. The XRD spectra (obtained using a wavelength of 1.54 Å) were generated using a Rigaku SmartLab diffractometer by scanning the samples from 10 to 75 degrees at 2° min<sup>-1</sup> coupled with a diffracted beam monochromator (DBM) to reduce sample fluorescence. An accelerating current and voltage of 44 mA and 40 kV, respectively, were applied for all the scans. The generated XRD spectra were analyzed using the Rigaku PDXL software and phase identification was carried out using the Joint Committee on Powder Diffraction Standards (JCPDS) database.

### 2.2 Thermogravimetric analysis

Prior to the thermogravimetric evaluation of the oxygen carrier samples through extended redox cycles, all the

samples were activated in H<sub>2</sub> for 5 consecutive redox cycles at 800 °C, wherein they were reduced in H<sub>2</sub> and oxidized in air. 15–20 mg of the activated sample was placed in an alumina crucible of a Setaram SETSYS thermogravimetric analyzer (TGA) for subjecting it to 15 continuous reduction–oxidation (redox) cycles. A CH<sub>4</sub>/He/N<sub>2</sub> gas mixture comprising of 25% CH<sub>4</sub> concentration was introduced into the TGA during the reduction step at a rate of 200 ml min<sup>-1</sup> for 5 min. Oxidation was carried out for 4 min using a gas stream with a total flowrate of 200 ml min<sup>-1</sup> and 10.5% O<sub>2</sub>, with N<sub>2</sub> as the balance gas. N<sub>2</sub>-Flushing was carried out between the reduction and oxidation steps for 2.5 min with a N<sub>2</sub> flowrate of 100 ml min<sup>-1</sup>. Additionally, experiments were also performed to evaluate the regeneration performance of the reduced oxygen carrier samples by sending in a gas mixture with a 200 ml min<sup>-1</sup> flowrate comprising of 25% CO<sub>2</sub>. This was done to assess the oxidation performance of the carriers using CO<sub>2</sub>, which can oxidize the reduced Ca<sub>2</sub>Fe<sub>2</sub>O<sub>5</sub> completely. Redox cycles were carried out at 750, 800, 900, and 1000 °C to evaluate the effect of temperature on the reducibility of Ca<sub>2</sub>Fe<sub>2-x</sub>Ni<sub>x</sub>O<sub>5</sub> using CH<sub>4</sub>. Eqn (2) and (3) were used to assess the weight change data during the reduction and oxidation (in both air and CO<sub>2</sub>), respectively.

$$\text{Solid conversion (R, \%)} = \frac{W_o - W_t}{W_o - W_r} \times 100\% \quad (2)$$

$$\text{Solid conversion (O, \%)} = \frac{W_{ro} - W_t}{W_o - W_r} \times 100\% \quad (3)$$

W<sub>o</sub>, W<sub>t</sub>, W<sub>r</sub>, and W<sub>ro</sub> refer to the weight of the fresh oxygen carrier sample placed in the TGA, weight of the sample after 5 min of reduction, weight of the fully reduced oxygen carrier, and weight of the regenerated oxygen carrier, respectively.

### 2.3 Density functional theory (DFT) calculations

The first-principles calculations were performed within the framework of DFT using VASP.<sup>36,37</sup> The Perdew–Burke–Ernzerhof generalized gradient approximation (PBE-GGA) was used to represent the exchange–correlation energy,<sup>38</sup> and the projector-augmented wave (PAW) method, with an energy cut-off of 400 eV, was applied to describe the wave functions of the atomic cores.<sup>39,40</sup> The 5 × 5 × 5 Monkhorst–Pack *k*-point mesh was used for bulk optimization, and the structures were optimized until the energy had sufficiently converged to 1.0 × 10<sup>-5</sup> eV per atom.

The oxygen vacancy formation energy per vacancy was calculated using the following equation:

$$E_f = \left[ \left( E_v + \frac{n}{2} E_{O_2} \right) - E_{tot} \right] / n \quad (4)$$

where, E<sub>tot</sub> and E<sub>v</sub> are the total energy of the stoichiometric surface and the reduced surface, respectively. E<sub>O<sub>2</sub></sub> is the energy of an isolated oxygen molecule and *n* is the number of oxygen vacancies.

The adsorption energy, E<sub>ad</sub>, was calculated as follows:

$$E_{ad} = E_A + E_{surf} - E_{(A+surf)} \quad (5)$$

where E<sub>surf</sub> is the total energy of the clean surface, E<sub>A</sub> is the total energy of an isolated adsorbate in the gas phase, and E<sub>(A+surf)</sub> is the total energy of the surface–adsorbate system. The climbing-image nudged elastic band (CI-NEB) method was used for reaction barrier calculations.<sup>41,42</sup>

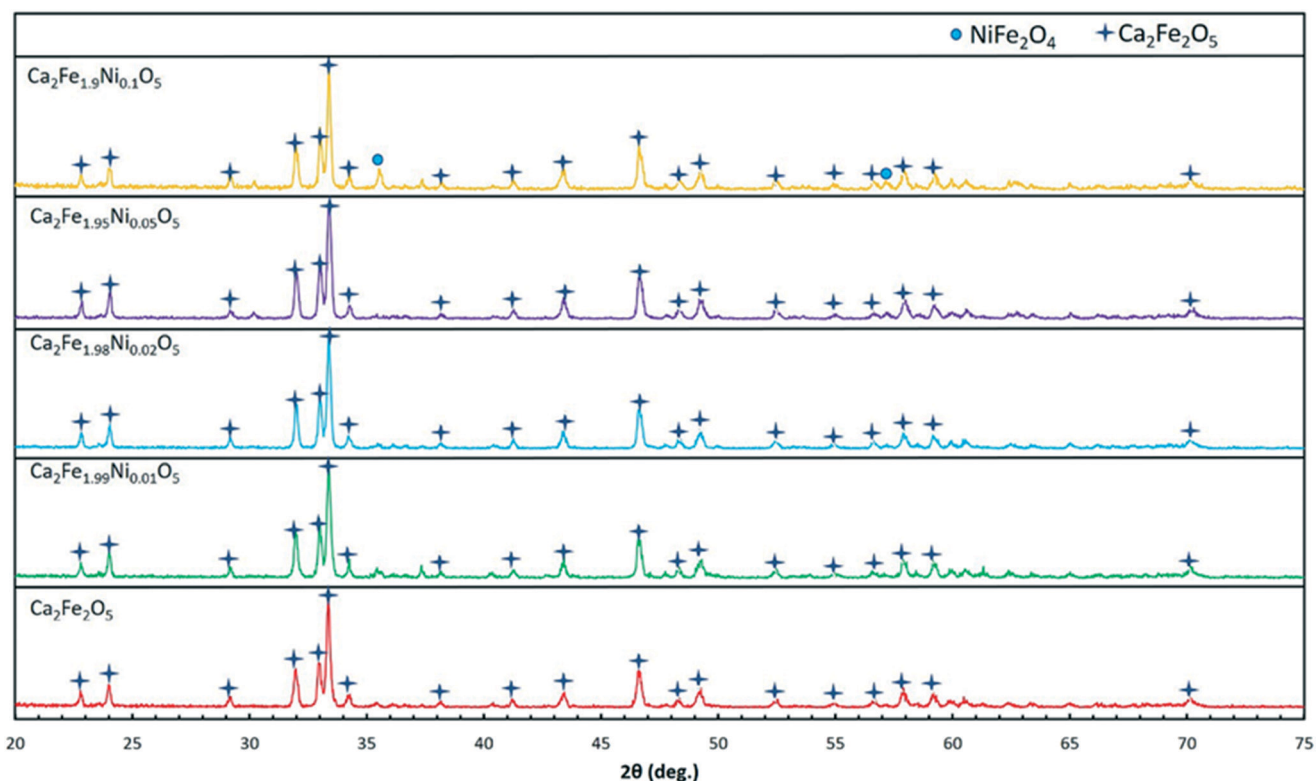
## 3. Results and discussion

Table 1 shows the different oxygen carriers synthesized along with their average grain size obtained from SEM imaging and phases identified using XRD. The XRD spectra obtained for the freshly synthesized oxygen carrier particles are shown in Fig. 2. As seen from the figure, a pure Ca<sub>2</sub>Fe<sub>2</sub>O<sub>5</sub> phase was obtained by varying the dopant concentration from 0 to 5%. As the Ni-dopant concentration was increased to 10%, formation of an impurity phase (NiFe<sub>2</sub>O<sub>4</sub>) took place as indicated in the XRD spectra. This finding suggested that the Ca<sub>2</sub>Fe<sub>2</sub>O<sub>5</sub> lattice became saturated at 10% Ni concentration. Until this doping level, the Fe atoms from Ca<sub>2</sub>Fe<sub>2</sub>O<sub>5</sub> could be effectively replaced by Ni atoms without any Fe–Ni interaction. However, increasing the doping concentration beyond 5% led to the formation of NiFe<sub>2</sub>O<sub>4</sub>, an unwanted phase that could alter the Ca<sub>2</sub>Fe<sub>2</sub>O<sub>5</sub> structure, thereby leading to decreased reactivity and hindering the CO<sub>2</sub> oxidation as the regeneration of the reduced Ni–Fe phase using CO<sub>2</sub> is thermodynamically inhibited. Shin *et al.* reported the formation of Fe<sub>3</sub>O<sub>4</sub> and metallic Ni upon oxidizing reduced NiFe<sub>2</sub>O<sub>4</sub>, while Huang *et al.* have also reported the occurrence of metallic Ni, Ni<sub>1-x</sub>Fe<sub>2+x</sub>O<sub>4</sub>, and Fe<sub>2+y</sub>O<sub>4</sub> phases upon CO<sub>2</sub> oxidation.<sup>43,44</sup> To carefully examine the effect of doping on the Ca<sub>2</sub>Fe<sub>2</sub>O<sub>5</sub> structure, the peak intensity corresponding to the doped and undoped samples was plotted by conducting XRD while varying the 2θ values from 31.6 to 32.4 degrees as shown in Fig. 3, which shows a peak shift for all the doped Ca<sub>2</sub>Fe<sub>2</sub>O<sub>5</sub> samples. As Ni<sup>2+</sup> (ionic radii = 69 pm) successfully replaced the Fe<sup>3+</sup> (ionic radii = 63 pm) atoms in the lattice, loss of oxygen takes place to maintain charge neutrality in the compound and therefore, the unit cell volume decreased.<sup>45</sup> Thus, a peak shift to the right was observed for the doped samples. Similarly, a change in the peak intensity was observed, which can be attributed to the difference of the electron density of the Fe-only lattice and the oxygen carrier lattice with the Fe–Ni atoms present in the doped samples. The surface morphology of the oxygen carrier samples was analyzed using SEM imaging. As seen from the micrographs shown in Fig. 4, the oxygen carriers with a doping concentration of ≤5% showed a similar granular morphology with no other visible microstructure. All the samples had a similar grain size in the range of 1–1.3 μm suggesting that the dopant addition did not change the physical attributes of the oxygen carrier. However, in Ca<sub>2</sub>Fe<sub>1.5</sub>–Ni<sub>0.1</sub>O<sub>5</sub>, two types of surface morphologies were observed as seen in Fig. 4e (also verified using energy dispersive X-ray spectroscopy). The growth of more porous NiFe<sub>2</sub>O<sub>4</sub> crystals

**Table 1** Characteristics of the doped and undoped samples used in this study

Sample no.	Sample name	Ni (dopant) concentration (mol%)	Average grain size ( $\mu\text{m}$ )	Major chemical phases <sup>a</sup>	Standard deviation ( $\mu\text{m}$ )
1	$\text{Ca}_2\text{Fe}_2\text{O}_5$	0	1.01	$\text{Ca}_2\text{Fe}_2\text{O}_5$	0.1
2	$\text{Ca}_2\text{Fe}_{1.99}\text{Ni}_{0.01}\text{O}_5$	1	1.29	$\text{Ca}_2\text{Fe}_2\text{O}_5$	0.11
3	$\text{Ca}_2\text{Fe}_{1.98}\text{Ni}_{0.02}\text{O}_5$	2	1.12	$\text{Ca}_2\text{Fe}_2\text{O}_5$	0.1
4	$\text{Ca}_2\text{Fe}_{1.95}\text{Ni}_{0.05}\text{O}_5$	5	1.06	$\text{Ca}_2\text{Fe}_2\text{O}_5$	0.12
5	$\text{Ca}_2\text{Fe}_{1.9}\text{Ni}_{0.1}\text{O}_5$	10	1.21	$\text{Ca}_2\text{Fe}_2\text{O}_5$ , $\text{NiFe}_2\text{O}_4$	0.1

<sup>a</sup> As identified by XRD.

**Fig. 2** XRD spectra of the doped and undoped oxygen carrier samples.

was observed on the  $\text{Ca}_2\text{Fe}_2\text{O}_5$  surface, thereby corroborating the results obtained from the XRD analysis.

Fig. 5 shows the solid conversion of the doped and undoped samples during the reduction at 900 °C. The doped samples performed significantly better than the undoped sample. In the CLPO process, oxygen carriers provide lattice oxygen to partially oxidize methane in the reducer reactor, thus leading to the formation of oxygen vacancies. Our previous study has demonstrated that the formation of oxygen vacancies plays an important role in the structure–activity relationship of oxygen carriers.<sup>20,46</sup> To gain a mechanistic insight into the Ni doping effect on the reactivity of calcium ferrite oxygen carriers, the formation of oxygen vacancies on undoped  $\text{Ca}_2\text{Fe}_2\text{O}_5$ , Ni doped  $\text{Ca}_2\text{Fe}_2\text{O}_5$  and  $\text{NiFe}_2\text{O}_4$  was investigated using DFT calculations.  $\text{Ca}_2\text{Fe}_2\text{O}_5$  has a brownmillerite-type structure with layers alternating between corner-sharing octahedra and tetrahedra. The doped  $\text{Ca}_2\text{Fe}_2\text{O}_5$  was built by replacing one Fe atom at the outermost layer with one Ni atom. The optimized structures

of the  $\text{Ca}_2\text{Fe}_{1.95}\text{Ni}_{0.05}\text{O}_5$  (001) slab and  $\text{NiFe}_2\text{O}_4$  (001) slab are shown in Fig. 6a. The oxygen vacancy formation energies ( $E_f$ ) of these slabs can be obtained from eqn (4), and the relationship between  $E_f$  and the number of oxygen vacancies is shown in Fig. 6b. It can be found that the oxygen vacancy formation energy increases with an increase in the number of oxygen vacancies. The  $E_f$  of  $\text{Ca}_2\text{Fe}_2\text{O}_5$  increases to 3.15 eV from 2.12 eV when the number of oxygen vacancies increase to 5 from 1.

For  $\text{Ca}_2\text{Fe}_{1.95}\text{Ni}_{0.05}\text{O}_5$ , the formation energy of the first oxygen vacancy is 1.72 eV, which is 0.4 eV lower than that for  $\text{Ca}_2\text{Fe}_2\text{O}_5$ . When the number of oxygen vacancies increases to 5, the  $E_f$  of  $\text{Ca}_2\text{Fe}_{1.95}\text{Ni}_{0.05}\text{O}_5$  is 0.96 eV lower than the  $E_f$  of the undoped slab. It indicates that the Ni doping significantly facilitates the formation of oxygen vacancies which favors the  $\text{CH}_4$  partial oxidation.<sup>47</sup> In the CLPO process,  $\text{CH}_4$  is dissociated to hydrogen and  $\text{CH}_x$  radicals over the oxygen carrier. Then, the  $\text{CH}_x$  radicals are oxidized by lattice oxygen to generate CO and  $\text{H}_2$ . The energy barrier for the first step

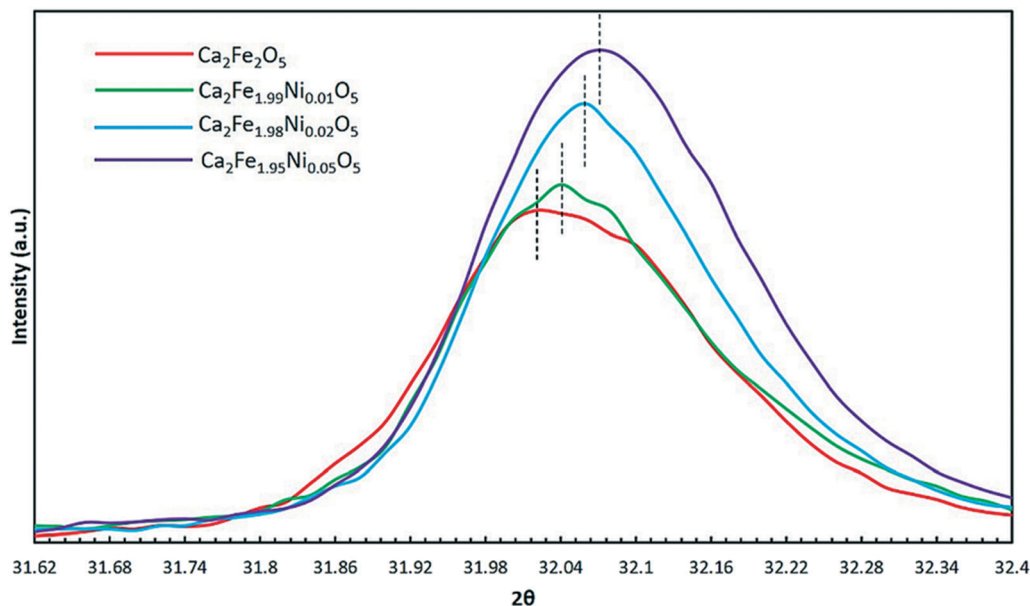


Fig. 3 XRD spectra obtained by varying the incident angle over a narrow range.

of  $\text{CH}_4$  dissociation on 5% Ni-doped  $\text{Ca}_2\text{Fe}_2\text{O}_5$  is  $152.7 \text{ kJ mol}^{-1}$ , which is  $36.5 \text{ kJ mol}^{-1}$  lower than that of  $\text{CH}_4$  dissociation on the undoped slab. The C–H bond cleavage barriers for  $\text{CH}_3$ ,  $\text{CH}_2$ , and  $\text{CH}$  on 5% Ni-doped  $\text{Ca}_2\text{Fe}_2\text{O}_5$  are  $95.1 \text{ kJ mol}^{-1}$ ,  $81.2 \text{ kJ mol}^{-1}$  and  $103.6 \text{ kJ mol}^{-1}$ , respectively, which are also lower than the corresponding barriers for the dissociation of these radicals on the undoped  $\text{Ca}_2\text{Fe}_2\text{O}_5$ .<sup>20</sup> These results agree with the experimental finding that the reactivity of Ni doped  $\text{Ca}_2\text{Fe}_2\text{O}_5$  is higher than that of the undoped sample. Among these slab models, the  $\text{NiFe}_2\text{O}_4$  (001) slab exhibits a high oxygen vacancy formation energy, implying its weak  $\text{CH}_4$  activation capability. In addition, the

calculated energy of adsorption for methane on the  $\text{NiFe}_2\text{O}_4$  surface is  $27.1 \text{ kJ mol}^{-1}$ , which is  $35.2 \text{ kJ mol}^{-1}$  lower than that for methane on the  $\text{Ca}_2\text{Fe}_2\text{O}_5$  surface. Therefore, the formation of  $\text{NiFe}_2\text{O}_4$  is unfavorable for the CLPO process.

Fig. 7 shows the comparison between the reduction and oxidation performance of  $\text{Ca}_2\text{Fe}_2\text{O}_5$  and  $\text{Ca}_2\text{Fe}_{1.95}\text{Ni}_{0.05}\text{O}_5$  across 15 continuous redox cycles at varying temperatures between 750 and 1000 °C. The reduction of the samples was carried out under 25%  $\text{CH}_4$  concentration whereas the reduced samples were oxidized in 10.5%  $\text{O}_2$ . As seen from Fig. 7, adding Ni as the dopant significantly increased the reduction and oxidation performance of  $\text{Ca}_2\text{Fe}_2\text{O}_5$  at all the temperatures. Adding 5% Ni to  $\text{Ca}_2\text{Fe}_2\text{O}_5$  increased the average solid conversion for reduction and oxidation by 1149% and 1147%, respectively at 750 °C as compared to the undoped sample. Similarly, the average solid conversion (reduction) showed an increase by 396%, 259%, and 190% at operating temperatures of 800 °C, 900 °C and 1000 °C, respectively, as shown in Fig. 7c, e and g. Likewise, the

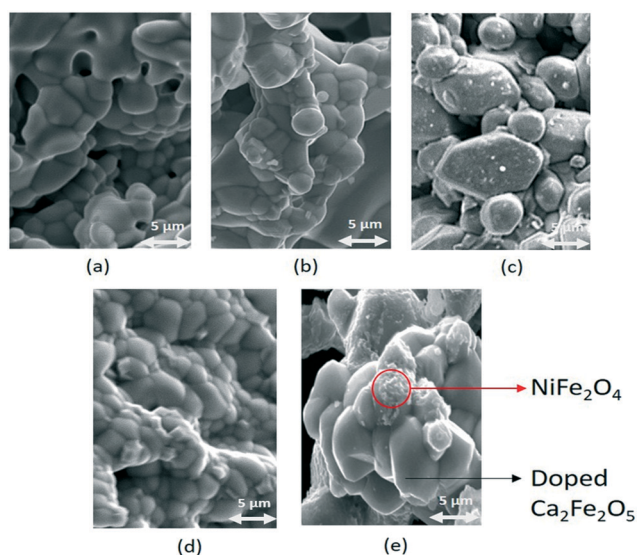


Fig. 4 Micrographs depicting the morphology of the (a)  $\text{Ca}_2\text{Fe}_2\text{O}_5$ , (b)  $\text{Ca}_2\text{Fe}_{1.99}\text{Ni}_{0.01}\text{O}_5$ , (c)  $\text{Ca}_2\text{Fe}_{1.98}\text{Ni}_{0.02}\text{O}_5$ , (d)  $\text{Ca}_2\text{Fe}_{1.95}\text{Ni}_{0.05}\text{O}_5$ , and (e)  $\text{Ca}_2\text{Fe}_{1.9}\text{Ni}_{0.1}\text{O}_5$  oxygen carrier samples.

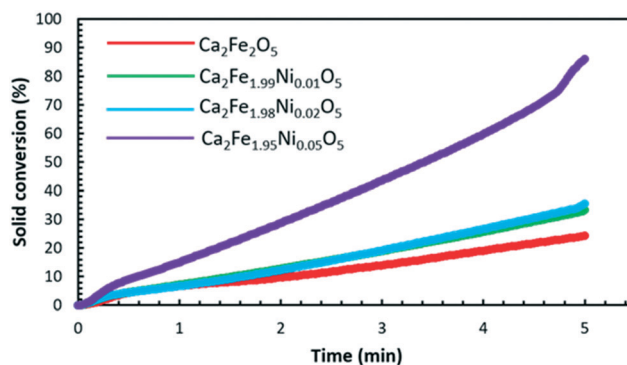
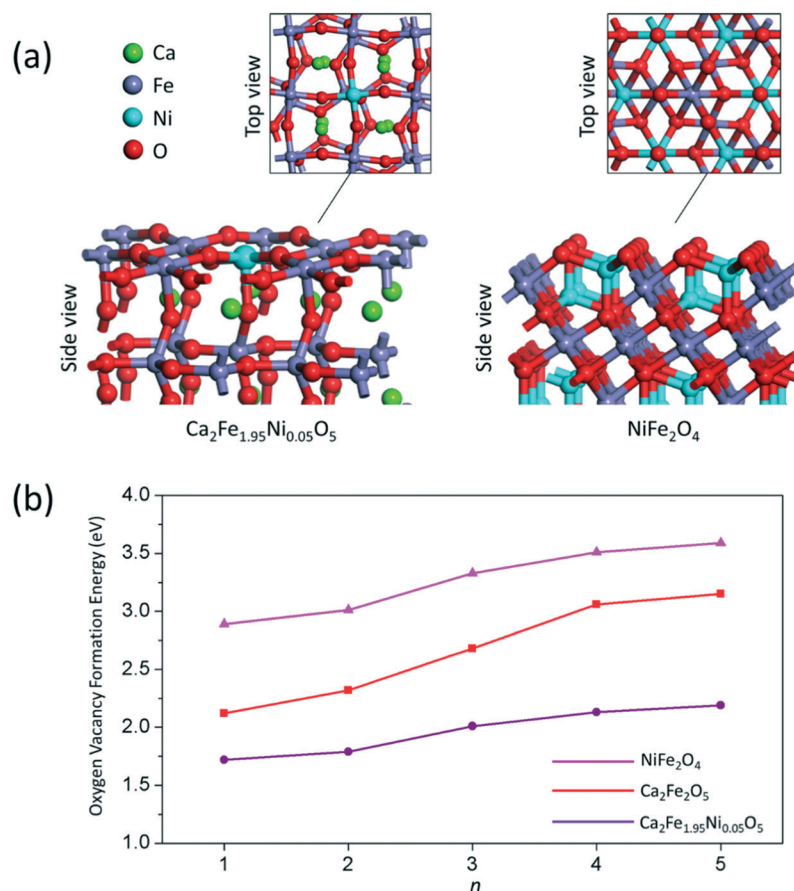


Fig. 5 Comparison of the reactivity (reduction) amongst the different oxygen carrier samples at 900 °C and 1 atm.



**Fig. 6** (a) Side view of the optimized structures of the  $\text{Ca}_2\text{Fe}_{1.95}\text{Ni}_{0.05}\text{O}_5$  slab and the  $\text{NiFe}_2\text{O}_4$  slab (the side view of the structures is shown in the inset); (b) the oxygen vacancy formation energies (eV) plotted as a function of the number of oxygen vacancies.

average solid conversion during the oxidation showed an enhancement by 397%, 259% and 190% corresponding to the temperatures of 800 °C, 900 °C and 1000 °C, respectively, for the 5% doped sample as compared to undoped  $\text{Ca}_2\text{Fe}_2\text{O}_5$  as depicted in Fig. 7d, f and h. It must be noted that at lower temperatures (750 °C and 800 °C), the steady state solid conversion is achieved after multiple redox cycles as opposed to higher temperatures (900 °C and 1000 °C) where it is reached within relatively less redox cycles. This behavior can be attributed to the impact of temperature on the reduction of the samples under given conditions, where the samples are still activating under  $\text{CH}_4$ . To further understand the effect of dopant addition on the redox performance of  $\text{Ca}_2\text{Fe}_2\text{O}_5$ , the dopant concentration was varied, and redox cycles were conducted at different temperatures. The change in the average values of solid conversion during the reduction and oxidation at different temperatures for varying dopant concentrations is shown in Fig. 8a and b, respectively. At 750 °C, increasing the dopant concentration from 0% to 1%, 2%, and 5% led to an increase in the reduction solid conversion by 238%, 237%, and 1149%, respectively. At 800 °C, the oxygen carrier samples with 1%, 2%, and 5% Ni showed an increase in the reduction performance by 59%, 58%, and 396% as compared to the undoped sample. Similarly, the

$\text{Ca}_2\text{Fe}_{1.99}\text{Ni}_{0.01}\text{O}_5$ ,  $\text{Ca}_2\text{Fe}_{1.98}\text{Ni}_{0.02}\text{O}_5$ , and  $\text{Ca}_2\text{Fe}_{1.95}\text{Ni}_{0.05}\text{O}_5$  samples showed an increase in the average reduction by 34%, 57%, and 259% and 10%, 21%, and 190% at 900 °C and 1000 °C, respectively, as compared to undoped  $\text{Ca}_2\text{Fe}_2\text{O}_5$ . The effect of the dopant on enhancing the reactivity by lowering the activation energy barrier is more prominent at lower temperatures as high temperature promotes reaction rates due to a strong effect on the rate constant.

One of the crucial advantages of  $\text{Ca}_2\text{Fe}_2\text{O}_5$  is its ability to be regenerated in steam/ $\text{CO}_2$  while producing  $\text{H}_2/\text{CO}$  as the products, thereby providing the flexibility to manipulate the  $\text{H}_2:\text{CO}$  ratio of the syngas produced in the reducer.<sup>22</sup> To assess the impact of Ni doping on the regeneration capability under  $\text{CO}_2$ , the doped and undoped samples were subjected to extended redox cycles using  $\text{CH}_4$  and  $\text{CO}_2$  as the reducing and oxidizing agents, respectively. Fig. 9a shows the oxidation performance of the different samples during  $\text{CO}_2$  oxidation at 750 and 900 °C. Similar to air oxidation, increasing the Ni concentration in the sample leads to a higher extent of oxidation. A better reduction performance across 15 redox cycles is also observed with  $\text{CO}_2$  as compared to air, as seen from Fig. 9b.

To elucidate the dopant effect on the  $\text{CO}_2$  conversion enhancement, the  $\text{CO}_2$  adsorption on the reduced  $\text{Ca}_2\text{Fe}_2\text{O}_5$

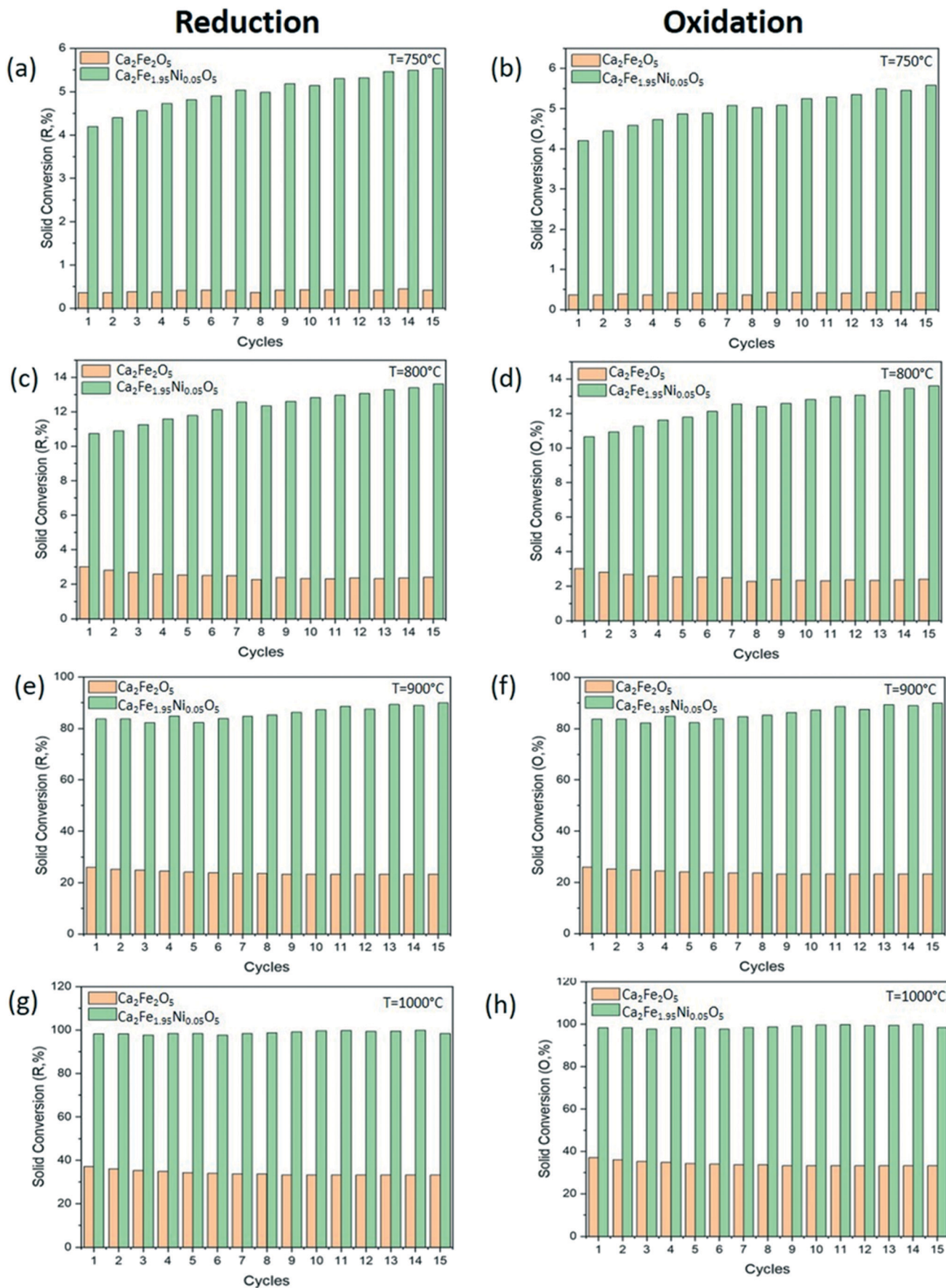


Fig. 7 Cyclic performance during the reduction (a, c, e and g) and air oxidation (b, d, f and h) of  $\text{Ca}_2\text{Fe}_2\text{O}_5$  and  $\text{Ca}_2\text{Fe}_{1.95}\text{Ni}_{0.05}\text{O}_5$  at different temperatures.



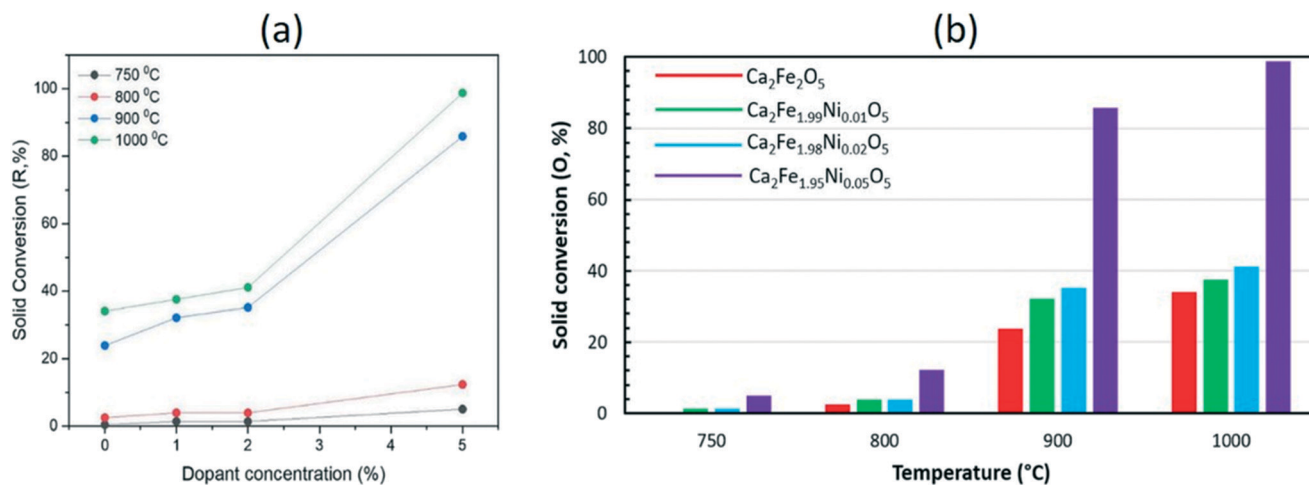


Fig. 8 Solid conversions during the (a) reduction and (b) oxidation of the oxygen carrier samples as a function of dopant concentration and temperature.

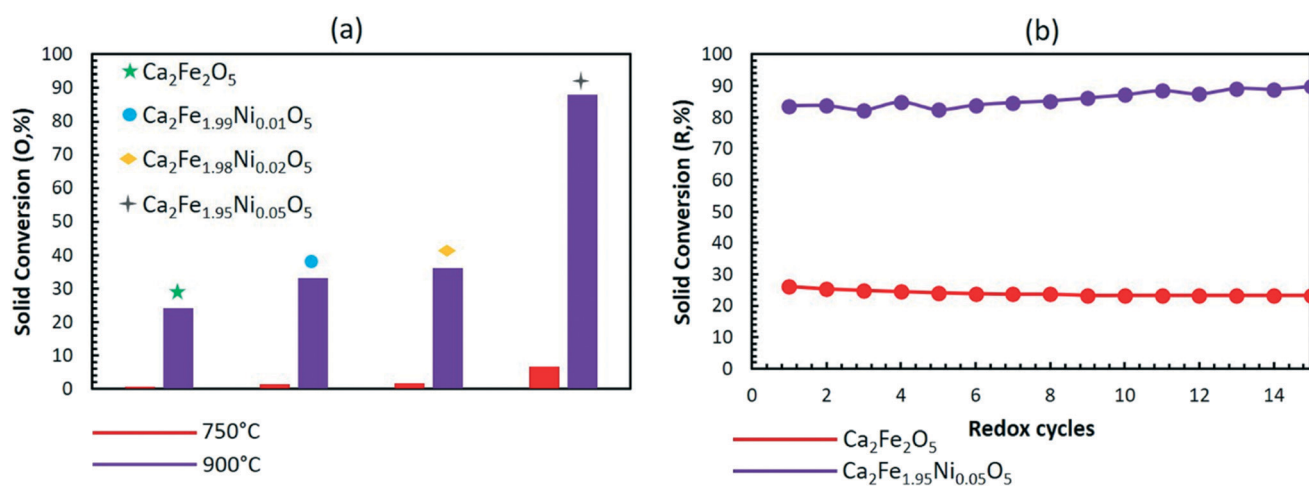


Fig. 9 (a) Solid conversion during the oxidation of the reduced sample with  $\text{CO}_2$  and (b) 15 isothermal  $\text{CH}_4\text{-CO}_2$  redox cycles at 900 °C and 1 atm.

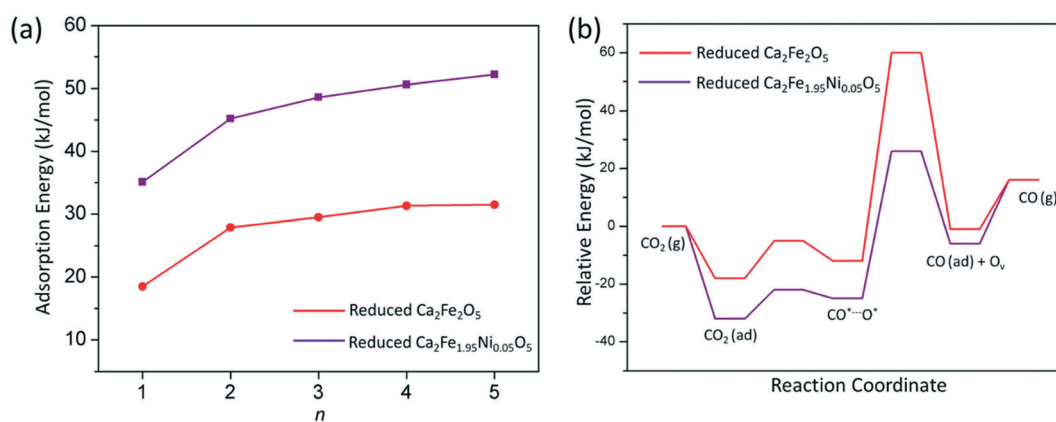


Fig. 10 (a) The relationship between the  $\text{CO}_2$  adsorption energy and the number of oxygen vacancies; (b) the energy profiles for the  $\text{CO}_2$  conversion to  $\text{CO}$  on the reduced  $\text{Ca}_2\text{Fe}_2\text{O}_5$  and  $\text{Ca}_2\text{Fe}_{1.95}\text{Ni}_{0.05}\text{O}_5$  slabs.  $\text{O}_v$  denotes the lattice oxygen in the surface.

and  $\text{Ca}_2\text{Fe}_{1.95}\text{Ni}_{0.05}\text{O}_5$  slabs with  $n$  oxygen vacancies was investigated. The relationship between the adsorption energies and the oxygen vacancy number is shown in Fig. 10a. It is seen that the  $\text{CO}_2$  adsorption energy increases with the increasing number of oxygen vacancies on these slabs. Compared with the reduced  $\text{Ca}_2\text{Fe}_{1.95}\text{Ni}_{0.05}\text{O}_5$ , the  $\text{CO}_2$  adsorption energy on the reduced  $\text{Ca}_2\text{Fe}_2\text{O}_5$  was  $\sim 20 \text{ kJ mol}^{-1}$  lower. Thus, the adsorbed  $\text{CO}_2$  at the Ni dopant site is more favorable to the  $\text{CO}_2$  conversion in the regeneration process of the oxygen carriers. Fig. 10b shows the energy profiles for the  $\text{CO}_2$  conversion to CO on the reduced  $\text{Ca}_2\text{Fe}_2\text{O}_5$  and reduced  $\text{Ca}_2\text{Fe}_{1.95}\text{Ni}_{0.05}\text{O}_5$  slabs. It was found that the C–O bond cleavage of  $\text{CO}_2$  on the reduced  $\text{Ca}_2\text{Fe}_2\text{O}_5$  needs to overcome a high barrier of  $72.3 \text{ kJ mol}^{-1}$ , which is noticeably larger than that on the reduced  $\text{Ca}_2\text{Fe}_{1.95}\text{Ni}_{0.05}\text{O}_5$  ( $51.1 \text{ kJ mol}^{-1}$ ). These calculation results indicate that Ni doping is beneficial not only for methane partial oxidation in the reducer, but also for  $\text{CO}_2$  adsorption and conversion in the regeneration process of calcium ferrite oxygen carriers, which is in good agreement with the TGA test.

## 4. Conclusion

Natural gas and  $\text{CO}_2$  are the major contributors to global warming. Utilizing natural gas and  $\text{CO}_2$  as feedstocks in a process to produce valuable products is thus advantageous from both the environmental and economic perspectives. Chemical looping partial oxidation (CLPO) provides a scheme for enabling such a process that converts these feedstocks. This study examined the usage of Ni-doped calcium ferrite as an oxygen carrier in the CLPO process, where the dopant concentration is varied from 0 to 10% per mol of the carrier. As the CLPO process intended for commercial applications tends to use an adiabatic system wherein no external heat source is provided, the operating temperature drops as the reaction proceeds, thereby lowering  $\text{CH}_4$  oxidation kinetics. However, Ni-doped  $\text{Ca}_2\text{Fe}_2\text{O}_5$  carriers exhibited an enhanced activity across a wide range of operating temperatures ( $750\text{--}1000 \text{ }^\circ\text{C}$ ), with the most substantial improvement of 1149% for a 5% doped sample as compared to the undoped sample at  $750 \text{ }^\circ\text{C}$ . The experimental performance was validated using DFT calculations, which showed the lowering of the oxygen vacancy formation energy in the range of 0.4 to 0.96 eV when switched to the 5% Ni-doped sample as compared to undoped  $\text{Ca}_2\text{Fe}_2\text{O}_5$ . The regeneration performance of the reduced carriers was assessed using both air and  $\text{CO}_2$  as the oxidizing media, where both the oxidizing agents achieved complete regeneration of the reduced oxygen carriers, with the doped samples exhibiting higher reaction rates across a wide range of operating temperatures. DFT calculations further revealed a higher  $\text{CO}_2$  adsorption energy and a lower C–O bond cleavage energy barrier for the reduced 5% Ni-doped  $\text{Ca}_2\text{Fe}_2\text{O}_5$  as compared to the undoped one. Doping  $\text{Ca}_2\text{Fe}_2\text{O}_5$  with Ni thus yields fast reaction kinetics that successfully convert methane in the

CLPO process to produce high-quality syngas, while simultaneously splitting  $\text{CO}_2$  to generate CO, making this process highly effective.

## Conflicts of interest

There are no conflicts to declare.

## Acknowledgements

The authors would like to acknowledge resources provided by the Center for Electron Microscopy and Analysis (CEMAS) and the Ohio Supercomputer Center (OSC) for carrying out electron microscopy and computational simulations, respectively. The help from Rushikesh Joshi with synthesizing the oxygen carrier samples is appreciated.

## References

- 1 L. Qin, Z. Cheng, D. Baser, T. Goldenbaum, J. A. Fan and L.-S. Fan, Cyclic Redox Scheme towards Shale Gas Reforming: A Review and Perspectives, *React. Chem. Eng.*, 2020, 5(12), 2204–2220, DOI: 10.1039/d0re00301h.
- 2 U.S. Energy Information Administration, Monthly Energy Review (July), 2020, <https://www.eia.gov/todayinenergy/detail.php?id=43675>, (accessed Aug 2, 2020).
- 3 Z. Cheng, D. S. Baser, S. G. Nadgouda, L. Qin, J. A. Fan and L.-S. Fan,  $\text{C}_2$  Selectivity Enhancement in Chemical Looping Oxidative Coupling of Methane over a Mg-Mn Composite Oxygen Carrier by Li-Doping-Induced Oxygen Vacancies, *ACS Energy Lett.*, 2018, 3(7), 1730–1736, DOI: 10.1021/acscenergylett.8b00851.
- 4 C. Park, T. L. Hsieh, Y. Pottimurthy, V. Shah, D. Xu, Y. Y. Chen, L.-S. Fan and A. Tong, Design and Operations of a 15 KWth Subpilot Unit for the Methane-to-Syngas Chemical Looping Process with  $\text{CO}_2$  Utilization, *Ind. Eng. Chem. Res.*, 2020, 59(15), 6886–6899, DOI: 10.1021/acs.iecr.9b05577.
- 5 L.-S. Fan, *Chemical Looping Partial Oxidation*, Cambridge University Press, 2017, DOI: 10.1017/9781108157841.
- 6 L. K. Rath, *Assessment of Hydrogen Production with  $\text{CO}_2$  Capture Volume 1: Baseline State-of-the-Art Plants*, DoE/NETL, Rep., 2010, 1434.
- 7 C. A. H. Price, L. Pastor-Pérez, T. R. Reina and J. Liu, Robust Mesoporous Bimetallic Yolk-Shell Catalysts for Chemical  $\text{CO}_2$  Upgrading via Dry Reforming of Methane, *React. Chem. Eng.*, 2018, 3(4), 433–436, DOI: 10.1039/c8re00058a.
- 8 R. C. Pattison and M. Baldea, Optimal Design of Air Separation Plants with Variable Electricity Pricing, in *Computer Aided Chemical Engineering*, 2014, DOI: 10.1016/B978-0-444-63433-7.50050-X.
- 9 L. Zeng, Z. Cheng, J. A. Fan, L.-S. Fan and J. Gong, Metal Oxide Redox Chemistry for Chemical Looping Processes, *Nat. Rev. Chem.*, 2018, 2(11), 349–364, DOI: 10.1038/s41570-018-0046-2.
- 10 A. Joshi, V. Shah, P. Mohapatra, S. Kumar, R. K. Joshi, M. Kathe, L. Qin, A. Tong and L.-S. Fan, Chemical Looping-A Perspective on the Next-Gen Technology for Efficient Fossil

- Fuel Utilization, *Advances in Applied Energy*, 2021, 100044, DOI: 10.1016/j.adapen.2021.100044.
- 11 S. Luo, L. Zeng, D. Xu, M. Kathe, E. Chung, N. Deshpande, L. Qin, A. Majumder, T.-L. Hsieh, A. Tong, Z. Sun and L.-S. Fan, Shale Gas-to-Syngas Chemical Looping Process for Stable Shale Gas Conversion to High Purity Syngas with a H<sub>2</sub>: CO Ratio of 2: 1, *Energy Environ. Sci.*, 2014, 7(12), 4104–4117, DOI: 10.1039/C4EE02892A.
  - 12 C. Chung, L. Qin, V. Shah and L.-S. Fan, Chemically and Physically Robust, Commercially-Viable Iron-Based Composite Oxygen Carriers Sustainable over 3000 Redox Cycles at High Temperatures for Chemical Looping Applications, *Energy Environ. Sci.*, 2017, 10(11), 2318–2323, DOI: 10.1039/c7ee02657a.
  - 13 L.-S. Fan, *Chemical Looping Systems for Fossil Energy Conversions*, John Wiley & Sons, Inc., Hoboken, NJ, USA, 2010, DOI: 10.1002/9780470872888.
  - 14 Y. Y. Chen, S. Nadgouda, V. Shah, L.-S. Fan and A. Tong, Oxidation Kinetic Modelling of Fe-Based Oxygen Carriers for Chemical Looping Applications: Impact of the Topochemical Effect, *Appl. Energy*, 2020, 279, 115701, DOI: 10.1016/j.apenergy.2020.115701.
  - 15 L. Qin, M. Guo, Y. Liu, Z. Cheng, J. A. Fan and L.-S. Fan, Enhanced Methane Conversion in Chemical Looping Partial Oxidation Systems Using a Copper Doping Modification, *Appl. Catal., B*, 2018, 235, 143–149, DOI: 10.1016/j.apcatb.2018.04.072.
  - 16 M. Guo, Z. Cheng, Y. Liu, L. Qin, J. Goetze, J. A. Fan and L.-S. Fan, Cobalt Doping Modification for Enhanced Methane Conversion at Low Temperature in Chemical Looping Reforming Systems, *Catal. Today*, 2020, 350, 156–164, DOI: 10.1016/j.cattod.2019.06.016.
  - 17 Y. Liu, L. Qin, Z. Cheng, J. W. Goetze, F. Kong, J. A. Fan and L.-S. Fan, Near 100% CO Selectivity in Nanoscaled Iron-Based Oxygen Carriers for Chemical Looping Methane Partial Oxidation, *Nat. Commun.*, 2019, 10(1), 1–6, DOI: 10.1038/s41467-019-13560-0.
  - 18 X. Zhang, Y. Su, C. Pei, Z. J. Zhao, R. Liu and J. Gong, Chemical Looping Steam Reforming of Methane over Ce-Doped Perovskites, *Chem. Eng. Sci.*, 2020, 223, 115707, DOI: 10.1016/j.ces.2020.115707.
  - 19 X. Zhang, C. Pei, X. Chang, S. Chen, R. Liu, Z. J. Zhao, R. Mu and J. Gong, FeO<sub>6</sub> Octahedral Distortion Activates Lattice Oxygen in Perovskite Ferrite for Methane Partial Oxidation Coupled with CO<sub>2</sub> Splitting, *J. Am. Chem. Soc.*, 2020, 142(26), 11540–11549, DOI: 10.1021/jacs.0c04643.
  - 20 V. Shah, Z. Cheng, D. S. Baser, J. A. Fan and L.-S. Fan, Highly Selective Production of Syngas from Chemical Looping Reforming of Methane with CO<sub>2</sub> Utilization on MgO-Supported Calcium Ferrite Redox Materials, *Appl. Energy*, 2021, 282, 116111, DOI: 10.1016/j.apenergy.2020.116111.
  - 21 D. Hirabayashi, T. Yoshikawa, K. Mochizuki, K. Suzuki and Y. Sakai, Formation of Brownmillerite Type Calcium Ferrite (Ca<sub>2</sub>Fe<sub>2</sub>O<sub>5</sub>) and Catalytic Properties in Propylene Combustion, *Catal. Lett.*, 2006, 110(1), 155–160, DOI: 10.1007/s10562-006-0120-0.
  - 22 V. Shah, P. Mohapatra and L.-S. Fan, Thermodynamic and Process Analyses of Syngas Production Using Chemical Looping Reforming Assisted by Flexible Dicalcium Ferrite-Based Oxygen Carrier Regeneration, *Energy Fuels*, 2020, 34(5), 6490–6500, DOI: 10.1021/acs.energyfuels.0c00479.
  - 23 V. Shah, R. Joshi and L.-S. Fan, Thermodynamic Investigation of Process Enhancement in Chemical Looping Reforming of Methane through Modified Ca–Fe Oxygen Carrier Utilization, *Ind. Eng. Chem. Res.*, 2020, 59(35), 15531–15541, DOI: 10.1021/acs.iecr.0c03062.
  - 24 Q. Hu, Y. Shen, J. W. Chew, T. Ge and C. H. Wang, Chemical Looping Gasification of Biomass with Fe<sub>2</sub>O<sub>3</sub>/CaO as the Oxygen Carrier for Hydrogen-Enriched Syngas Production, *Chem. Eng. J.*, 2020, 379, 122346, DOI: 10.1016/j.cej.2019.122346.
  - 25 Y. Wang, P. Niu and H. Zhao, Chemical Looping Gasification of Coal Using Calcium Ferrites as Oxygen Carrier, *Fuel Process. Technol.*, 2019, 192, 75–86, DOI: 10.1016/j.fuproc.2019.04.009.
  - 26 B. Bhui and V. Prabu, Chemical Looping Based Co-Combustion of High Ash Indian Coal and Rice Straw Operating under CO<sub>2</sub> in-Situ Gasification Mode, *J. Energy Inst.*, 2021, 94, 176–190, DOI: 10.1016/j.joei.2020.07.004.
  - 27 W. Cuiping, Y. Hao, Y. Yanbo, L. Wenzheng, Y. Shirui, C. Weiwei, W. Fengyin, B. Hongcun and H. Xiude, Chemical Looping Reforming of Coal Tar Vapor on the Surface of CaO-Modified Fe-Based Oxygen Carrier, *Energy Fuels*, 2020, 34(7), 8534–8542, DOI: 10.1021/acs.energyfuels.0c00839.
  - 28 G. Liu, Y. Liao, Y. Wu and X. Ma, Reactivity of Co-Doped Ca<sub>2</sub>-Fe<sub>2</sub>O<sub>5</sub> Brownmillerite Oxides as Oxygen Carriers for Microalgae Chemical Looping Gasification, *Int. J. Hydrogen Energy*, 2019, 44(5), 2546–2559, DOI: 10.1016/j.ijhydene.2018.11.232.
  - 29 D. D. Miller, J. Riley and R. Siriwardane, Interaction of Methane with Calcium Ferrite in the Chemical Looping Partial Oxidation Application: Experimental and DFT Study, *Energy Fuels*, 2020, 34(2), 2193–2204, DOI: 10.1021/acs.energyfuels.9b03623.
  - 30 R. K. Joshi, V. Shah and L.-S. Fan, Acetic Acid Production Using Calcium Ferrite-Assisted Chemical Looping Gasification of Petroleum Coke With In Situ Sulfur Capture, *Energy Fuels*, 2020, 34(12), 16560–16571, DOI: 10.1021/acs.energyfuels.0c03408.
  - 31 G. Liu, Y. Liao, Y. Wu and X. Ma, Evaluation of Sr-Substituted Ca<sub>2</sub>Fe<sub>2</sub>O<sub>5</sub> as Oxygen Carrier in Microalgae Chemical Looping Gasification, *Fuel Process. Technol.*, 2019, 191, 93–103, DOI: 10.1016/j.fuproc.2019.03.019.
  - 32 D. Hosseini, F. Donat, P. M. Abdala, S. M. Kim, A. M. Kierzkowska and C. R. Müller, Reversible Exsolution of Dopant Improves the Performance of Ca<sub>2</sub>Fe<sub>2</sub>O<sub>5</sub> for Chemical Looping Hydrogen Production, *ACS Appl. Mater. Interfaces*, 2019, 11(20), 18276–18284, DOI: 10.1021/acsami.8b16732.
  - 33 G. Liu, Y. Liao, Y. Wu and X. Ma, Enhancement of Ca<sub>2</sub>Fe<sub>2</sub>O<sub>5</sub> Oxygen Carrier through Mg/Al/Zn Oxide Support for Biomass Chemical Looping Gasification, *Energy Convers. Manage.*, 2019, 195, 262–273, DOI: 10.1016/j.enconman.2019.04.087.
  - 34 M. V. Kathe, A. Empfield, J. Na, E. Blair and L.-S. Fan, Hydrogen Production from Natural Gas Using an Iron-Based

- Chemical Looping Technology: Thermodynamic Simulations and Process System Analysis, *Appl. Energy*, 2016, **165**, 183–201, DOI: 10.1016/j.apenergy.2015.11.047.
- 35 S. Wilbur, M. Williams, R. Williams, F. Scinicariello, J. M. Klotzbach, G. L. Diamond and M. Citra, *Toxicological Profile for Carbon Monoxide*, U.S. Agency Toxic Subst. Dis. Regist., 2012.
- 36 G. Kresse and J. Furthmüller, Efficiency of Ab-Initio Total Energy Calculations for Metals and Semiconductors Using a Plane-Wave Basis Set, *Comput. Mater. Sci.*, 1996, **6**(1), 15–50, DOI: 10.1016/0927-0256(96)00008-0.
- 37 G. Kresse and J. Furthmüller, Efficient Iterative Schemes for Ab Initio Total-Energy Calculations Using a Plane-Wave Basis Set, *Phys. Rev. B: Condens. Matter Mater. Phys.*, 1996, **54**(16), 11169, DOI: 10.1103/PhysRevB.54.11169.
- 38 J. P. Perdew, K. Burke and M. Ernzerhof, Generalized Gradient Approximation Made Simple, *Phys. Rev. Lett.*, 1996, **77**(18), 3865, (*Phys. Rev. Lett.*, 1997, **78**(7), 1396–1396), DOI: 10.1103/PhysRevLett.78.1396.
- 39 P. E. Blöchl, Projector Augmented-Wave Method, *Phys. Rev. B*, 1994, **50**(24), 17953, DOI: 10.1103/PhysRevB.50.17953.
- 40 G. Kresse and D. Joubert, From Ultrasoft Pseudopotentials to the Projector Augmented-Wave Method, *Phys. Rev. B*, 1999, **59**(3), 1758–1775, DOI: 10.1103/PhysRevB.59.1758.
- 41 G. Henkelman, B. P. Uberuaga and H. Jónsson, A Climbing Image Nudged Elastic Band Method for Finding Saddle Points and Minimum Energy Paths, *J. Chem. Phys.*, 2000, **113**(22), 9901–9904, DOI: 10.1063/1.1329672.
- 42 G. Henkelman and H. Jónsson, Improved Tangent Estimate in the Nudged Elastic Band Method for Finding Minimum Energy Paths and Saddle Points, *J. Chem. Phys.*, 2000, **113**(22), 9978–9985, DOI: 10.1063/1.1323224.
- 43 Z. Huang, H. Jiang, F. He, D. Chen, G. Wei, K. Zhao, A. Zheng, Y. Feng, Z. Zhao and H. Li, Evaluation of Multi-Cycle Performance of Chemical Looping Dry Reforming Using CO<sub>2</sub> as an Oxidant with Fe-Ni Bimetallic Oxides, *J. Energy Chem.*, 2016, **25**(1), 62–70, DOI: 10.1016/j.jechem.2015.10.008.
- 44 H. C. Shin, S. C. Choi, K. D. Jung and S. H. Han, Mechanism of M Ferrites (M = Cu and Ni) in the CO<sub>2</sub> Decomposition Reaction, *Chem. Mater.*, 2001, **13**(4), 1238–1242, DOI: 10.1021/cm000658b.
- 45 N. V. Dang, T. D. Thanh, L. V. Hong, V. D. Lam and T.-L. Phan, Structural, Optical and Magnetic Properties of Polycrystalline BaTi<sub>1-x</sub>Fe<sub>x</sub>O<sub>3</sub> Ceramics, *J. Appl. Phys.*, 2011, **110**(4), 043914, DOI: 10.1063/1.3625235.
- 46 L. Qin, Z. Cheng, J. A. Fan, D. Kopechek, D. Xu, N. Deshpande and L.-S. Fan, Nanostructure Formation Mechanism and Ion Diffusion in Iron-Titanium Composite Materials with Chemical Looping Redox Reactions, *J. Mater. Chem. A*, 2015, **3**(21), 11302–11312, DOI: 10.1039/C5TA01853F.
- 47 Z. Cheng, L. Qin, M. Guo, M. Xu, J. A. Fan and L.-S. Fan, Oxygen Vacancy Promoted Methane Partial Oxidation over Iron Oxide Oxygen Carriers in the Chemical Looping Process, *Phys. Chem. Chem. Phys.*, 2016, **18**(47), 32418–32428, DOI: 10.1039/c6cp06264d.